

RESEARCH ARTICLE | DECEMBER 11 2024

Reconstruction of soft x-ray emission in MAST Upgrade

Special Collection: [Proceedings of the 25th Topical Conference on High-Temperature Plasma Diagnostics](#)

B. A. Steward   ; M. Cecconello  ; C. Bowman; MAST-U Team



Rev. Sci. Instrum. 95, 123508 (2024)

<https://doi.org/10.1063/5.0219168>



Articles You May Be Interested In

Determination of hydrogen/deuterium ratio with neutron measurements on MAST

Rev. Sci. Instrum. (July 2014)

First measurements of energetic protons in Mega Amp Spherical Tokamak Upgrade (MAST-U)

Rev. Sci. Instrum. (August 2024)

Linear gyrokinetic simulations of toroidal Alfvén eigenmodes in the Mega-Amp Spherical Tokamak

Phys. Plasmas (November 2024)



Special Topics Open for Submissions

[Learn More](#)

Reconstruction of soft x-ray emission in MAST Upgrade

Cite as: Rev. Sci. Instrum. 95, 123508 (2024); doi: 10.1063/5.0219168

Submitted: 15 May 2024 • Accepted: 19 November 2024 •

Published Online: 11 December 2024



View Online



Export Citation



CrossMark

B. A. Steward,^{1,a)}  M. Cecconello,^{1,b)}  C. Bowman,² and MAST-U Team^{c)}

AFFILIATIONS

¹Durham University, Department of Physics, Durham DH1 3LE, United Kingdom

²UKAEA, Culham Centre for Fusion Energy, Culham OX14 3EB, United Kingdom

Note: This paper is part of the Special Topic on Proceedings of the 25th Topical Conference on High-Temperature Plasma Diagnostics.

^{a)}**Author to whom correspondence should be addressed:** Brian.Steward@durham.ac.uk

^{b)}**Also at:** Department of Physics and Astronomy, Uppsala University, Uppsala SE-751, Sweden.

^{c)}Harrison *et al.*, Nucl. Fusion **59**, 11201 (2019).

ABSTRACT

Understanding the confinement of fast ions is crucial for plasma heating and non-inductive current drive, i.e., for the operation of a fusion reactor. Interactions between fast ions and magnetohydrodynamic instabilities can reduce the performance of fusion reactions. Measuring the spatial shape and amplitude is crucial for constraining numerical modeling of the interaction between fast ions and these instabilities. Soft x rays can be used to study these magnetic instabilities. In particular, SXR tomography is used to reconstruct the two-dimensional profile of the SXR emissivity requiring only line integrated measurements, thus providing the spatial structure of the instabilities. This work presents SXR tomography reconstruction performed on synthetic SXR emissions from the Mega Ampere Spherical Tokamak Upgrade device. The synthetic SXR emissions are derived from time dependent tokamak transport data analysis code (TRANSP/NUBEAM) simulations. Different tomographic reconstruction models are compared, and the effect of two additional fans of intersecting lines of sight on the reconstructions' performances is investigated. The additional intersecting lines of sight greatly improve the accuracy of the reconstructions.

© 2024 Author(s). All article content, except where otherwise noted, is licensed under a Creative Commons Attribution (CC BY) license (<https://creativecommons.org/licenses/by/4.0/>). <https://doi.org/10.1063/5.0219168>

I. INTRODUCTION

A major challenge in magnetically confined fusion plasmas is the confinement of particles. Magnetohydrodynamic (MHD) instabilities can cause a decrease in the performance of a fusion plasma, or worse, a total loss of confinement of the plasma. Of particular interest is the interaction of MHD instabilities with supra-thermal particles called Fast Ions (FIs).¹ Fast ions can be produced from neutral beam injection (NBI) and ion cyclotron heating and as fusion reaction products.² In the Mega Ampere Spherical Tokamak Upgrade (MAST-U), FIs are predominantly generated by two tangential NBIs, one of which is aligned on-axis (aimed at the mid-plane of the tokamak) and the other is aligned off-axis (65 cm above the equatorial plane).³ These FIs are subjected to resonant and non-resonant instabilities: resonant MHD instabilities have frequencies similar to the frequency of both trapped and passing FIs, and

typical examples are Fish-Bones (FBs), Toroidal Alfvén Eigenmodes (TAEs), and Global Alfvén Eigenmodes (GAEs).⁴ In order to understand the interplay between FIs and instabilities and therefore reduce the loss of fast ions, the amplitude and spatial structure of the instabilities in the plasma core are required to correctly model the location and strength of the interaction. The experimental measurement of the perturbations in the plasma core is quite challenging, and most simulation codes rely on estimates of the perturbation via a combination of ideal MHD stability codes, such as MISHKA⁵ and NOVA,⁶ constrained by external magnetic pickup coil measurements. These resonant instabilities cause perturbations in the electron density and temperature and therefore in the soft x-ray (SXR) emission, which can then be used to infer the perturbations' spatial and temporal evolution in the plasma core. [Figure 1](#) shows an example of the FBs' signature on the SXR emission measured using a tangential array of detectors in MAST pulse 29976. As it can be seen, the

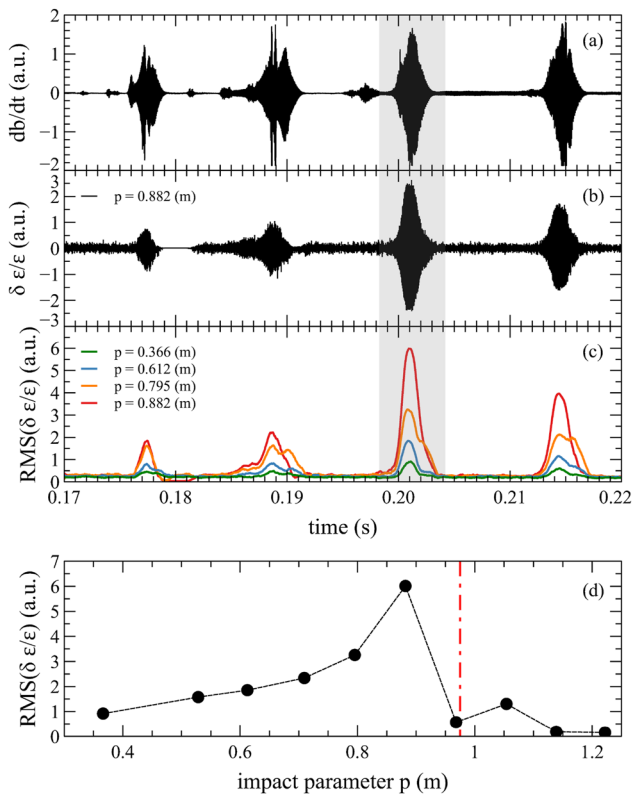


FIG. 1. Example of FBs in MAST plasma discharge No. 29 976. (a) Magnetic perturbation as measured using the OMAHA pickup coils, (b) bandpass filtered (10–130 kHz) tangential SXR signal near the magnetic axis ($p = 0.088$ m), (c) RMS of the bandpass filtered SXR signal at different impact parameter positions, and (d) radial profile of the maximum RMS in the shaded time interval in panels (a)–(c) for selected channels. The vertical red dashed line indicates the position of the magnetic axis. Here, the impact parameter measures the shortest distance between the line of sight and the central column of the tokamak.

root mean square (RMS) value of the relative fluctuation in the SXR emissivity depends on the spatial location of the emission providing a line integrated estimate of the perturbation amplitude. In order to reconstruct the 2D structure of such instabilities, tomographic methods are usually employed. The aim of this work is to assess the tomographic capabilities of the current SXR diagnostic installed on MAST-U (Secs. I–III) and to discuss the necessary improvements in the geometry and the number of sight lines required to reconstruct the unperturbed equilibrium (i.e., without MHD effects included). This is done using synthetic SXR data without the presence of MHD instabilities obtained from TRANSP/NUBEAM simulations of selected plasma scenarios characterized by different emissivity profiles (in this case due to on- and off-axis NBI heating). This first step is essential before perturbed synthetic SXR emissivity profiles can be properly reconstructed using the tomographic methods discussed here, which will be part of a following study.

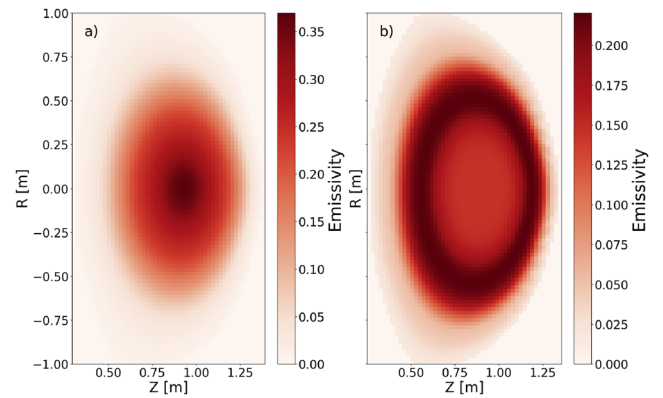


FIG. 2. Two synthetic SXR emissivity profiles. Panel (a) features on-axis heating creating a central hotspot, and panel (b) features off-axis heating creating a ring shaped hotspot.

II. SOFT X RAYS

Soft x rays have typical energies in the range of 0.1–20 keV and are typically due to bremsstrahlung radiation in plasmas with no impurities. Line radiation from impurities in the plasma can also occur in this range.⁷ Bremsstrahlung emission depends on plasma temperature, density, and effective charge Z_{eff} according to the relation⁷

$$\epsilon_{\text{SXR}} \propto n_e^2 Z_{\text{eff}} \sqrt{\frac{1}{T_e}}, \quad (1)$$

where n_e is the electron density, Z_{eff} is the effective charge, T_e is the electron temperature of the plasma, and ϵ_{SXR} is the emissivity.

Synthetic SXR emissivity (an example of which is shown in Fig. 2) is used to test the various tomographic methods. Figure 2(a) depicts the emissivity of a plasma when on-axis NBI heating is employed. This type of heating creates a central hotspot. Figure 2(b) shows an emissivity from a plasma with off-axis heating. The off-axis heating creates a hollow profile with a ring shaped hotspot. Both of these profiles are simulated by TRANSP/NUBEAM. Figure 2(a) shows a simulation following MAST-U shot 47 014, and Fig. 2(b) models MAST-U shot 43 666. The two emissivity profiles are chosen because the different features in the SXR emissions allow the robustness of the various reconstruction methods to be tested. An integration of the SXR emissivity along each of the lines of sight of the cameras is also performed to mimic the measurements of the SXR cameras currently in use on MAST-U. The line integrated emissivity along each line of sight (LoS) is then used in reconstructions of two-dimensional images via tomography.

III. CURRENT SXR CAMERAS ON MAST-U

MAST-U currently has two SXR cameras with 14 LoSs each. The cameras operate in a pinhole style and are composed of photodiodes.⁸ The LoSs intersect the plasma in a poloidal plane providing full coverage of the core of the plasma, as shown in the schematic

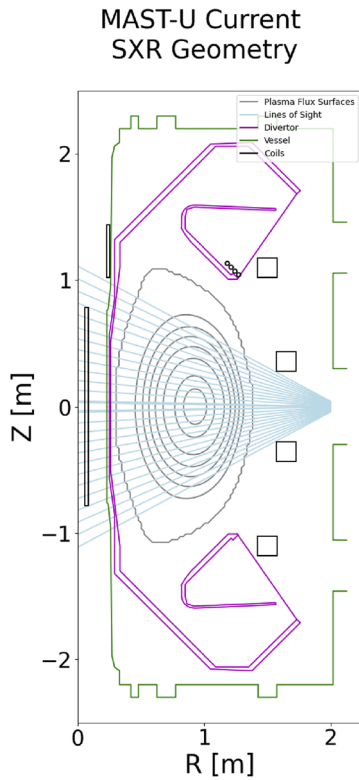


FIG. 3. Current array of SXR LoSs on the MAST-U device. The SXR cameras are situated in the mid-port of the vessel. The vessel is shown in green. The LoSs, shown in blue, fan out between two poloidal coils, which are shown in black.

in Fig. 3. As it can be seen, there are currently no intersecting lines of sight. While non-intersecting SXR LoSs are useful for Abel inversions,⁹ adding intersecting LoSs improves both the accuracy of the tomographic reconstruction of the SXR emissivity and the confidence in the reconstruction's accuracy. The accuracy improves in that the reconstructed emissivity will be closer to the synthetic one used for testing. The confidence in the reconstruction improves as further lines of sight are added to the reconstruction. One way to verify this is to compare the integrated lines of sight of the synthetic emissivity with the integrated lines of sight from the reconstructed emissivity.

IV. TOMOGRAPHY

Tomography is the method of reconstructing higher-dimensional (e.g., two- or three-dimensional) fields from line integrated measurements. The general tomographic problem is given by the following equation:¹⁰

$$f = T \cdot \varepsilon. \quad (2)$$

In the case of SXR tomography, ε is the reconstructed emissivity, f is the measurements from each of the camera LoSs, and T accounts for the length of each LoS in pixels that the LoS crosses.

Equation (2) cannot be generally solved, as it is under-determined. The solution can be approximated numerically by minimizing the square of the norm of the error $\chi = T \cdot \varepsilon - f$, thus minimizing the distance between the integrated lines of sight of the reconstruction ($T \cdot \varepsilon$) and the integrated lines of sight of the synthetic emissivity (f). To solve this problem, it is necessary to add some information about the form of the solution. This can be done by using the following equation:¹⁰

$$\Phi^2 = \frac{1}{2}\chi^2 + \alpha H, \quad (3)$$

where α is a free parameter that determines the magnitude of the effect of H on the final solution, Φ^2 is the variable that will be minimized to give a solution, and H is the added information and can come in many different forms, such as from the correlation of neighboring pixels by smoothing their first or second derivatives. α , as a free parameter, must be fixed by some method. To set the parameter in this case, the tomography is run repeatedly sweeping across values of α . At each instance of α , the least squares error between the reconstruction and the synthetic emissivity is calculated. The value determined via this method is 1×10^{-11} , as it is near the minima of the normalized least squares error for the methods shown here. This method works for synthetic tomography, when the emissivity profile is known beforehand, but is not possible when using experimental data, as there is no way of knowing the actual emissivity profile. In future work, this parameter can be set by Bayesian methods¹¹ or by more traditional methods, such as the discrepancy principle.¹² To minimize the function in Eq. (3), the derivative of Φ^2 is taken with respect to ε . Doing so results in the following equation:

$$(T^T \cdot T + \alpha H) \cdot \varepsilon = T^T \cdot f. \quad (4)$$

This form is a computationally convenient way to solve for the reconstructed profile ε .

First derivative smoothing is one way to add information to the system. In this method, H is a matrix that takes the spatial derivative of the emissivity, using a finite difference approximation. This serves to correlate adjacent pixels with each other and creates a smoothing effect. This is not addressed in this paper as it is not as effective at reconstruction as the techniques that are shown here.

A. Second derivative smoothing

The method of second derivative smoothing uses an H set to be the second spatial derivative of the emissivity. With this method of smoothing, pixels are correlated with themselves and with the adjacent pixels, resulting in a reconstruction that is smooth. The results of applying this method to reconstructing the SXR emissivity in the on- and off-axis NBI scenarios are shown in Fig. 4 [panels (a) and (b), respectively]. Qualitatively, there is an improved localization of the emissivity in the radial direction in the case of on-axis NBI heating [Fig. 4(a)]. For the off-axis case, Fig. 4(b), the annular structure of the emissivity is still not correctly identified. The normalized least squares error between the synthetic data and the reconstruction in Fig. 4(a) is 0.0255. Figure 4(b) shows a normalized least squares error of 0.0304.

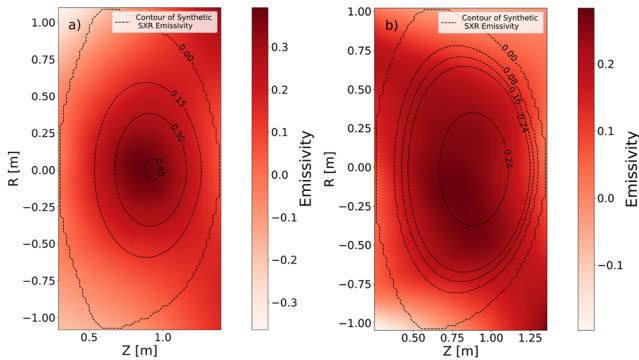


FIG. 4. Two reconstructed SXR emissivity profiles using second derivative smoothing and the current array of SXR LoSs. Panel (a) features on-axis heating, and panel (b) features off-axis heating. The contours indicate the synthetic emissivity that (a) and (b) reconstruct.

B. Minimum Fisher information

The next method of smoothing uses an iterative method to find the reconstructed image. The minimum Fisher information method uses the following equation to add information to Eq. (3):¹³

$$H = \int \frac{(\nabla \varepsilon)^2}{\varepsilon} dS. \quad (5)$$

In the above equation, ∇ is the spatial gradient function and dS is the differential element for a surface integral. As it can be seen in the above equation, the reconstructed ε is in the denominator, and therefore, the regions of stronger emissivity have less smoothing than the areas of lower emissivity. This means that features in high emissivity areas are less smoothed than in the previous method and will reveal their structure with more clarity. In the minimum Fisher iteration, an initial guess of a constant emissivity of value one is used for the emissivity in the denominator of Eq. (5) and the numerator is then calculated. The reconstructed emissivity in this iteration becomes the emissivity in the denominator of Eq. (5) for the following iteration. This process is repeated until the sum of squared

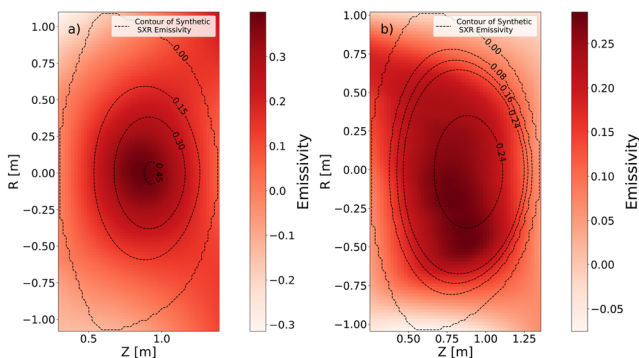


FIG. 5. Two reconstructed SXR emissivity profiles using minimum Fisher smoothing and the current array of SXR LoSs. Panel (a) features on-axis heating, and panel (b) features off-axis heating. The contours indicate the synthetic emissivity that (a) and (b) reconstruct.

distances between the two emissivities is less than 0.001, which is typically achieved in less than ten iterations. The reconstruction of the SXR emissivity using minimum Fisher information is shown in Fig. 5, again for both the on- and off-axis NBI heating scenarios. This method improves upon the second derivative method. The structure in Fig. 5(b) remains poorly resolved. In the case of on-axis NBI heating, [Fig. 5(a)], the reconstructed SXR emissivity is qualitatively close to the original synthetic data shown in Fig. 2(a). As for the off-axis NBI heating [Fig. 5(b)], the reconstructed SXR emissivity has a slight improvement over the second derivative method. The normalized least squares error between the synthetic data and Fig. 5(a) is 0.0177, and the error for Fig. 5(b) is 0.0275.

C. Additional lines of sight

As shown in Sec. IV B, more information is needed to correctly reconstruct the SXR emissivity, especially in the case of off-axis NBI heating. The current set of SXR LoSs in MAST-U shown in Fig. 3 is non-intersecting and is not very numerous. In this section, the effect of additional lines of sight on the poloidal plane on the SXR emissivity reconstruction is investigated. Figures 6(a) and 6(b) show an additional 28 and 54 LoSs, respectively. The number of additional LoSs is chosen such that SXR cameras of the type that is already present on MAST-U could be used. The additional 28 LoSs correspond to two additional cameras of the type that is currently employed, and the additional 54 LoSs correspond to four additional

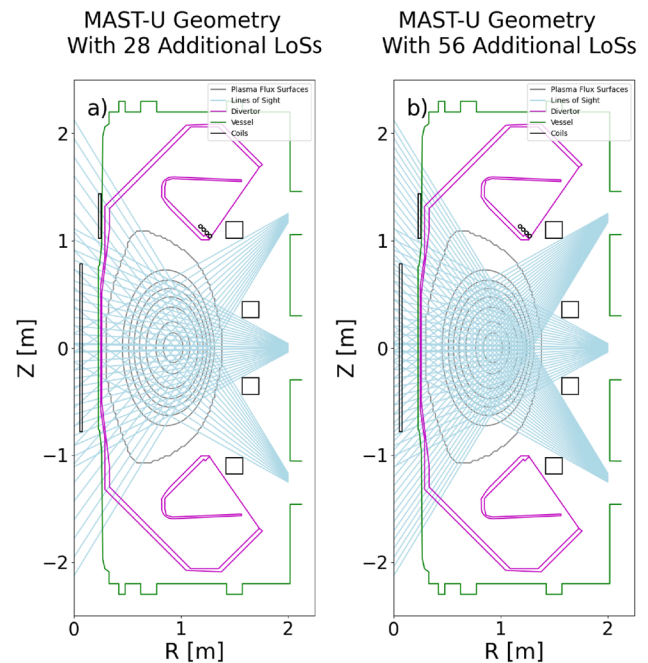


FIG. 6. Proposed additional SXR cameras on MAST-U in both (a) and (b). The new arrays are situated in ports in the vacuum vessel, shown in green. The upper and lower lines of sight see the plasma from between poloidal field coils, shown in black. In panel (a), 14 upper and lower lines of sight are added, and in panel (b), 28 upper and lower lines of sight are added.

TABLE I. Normalized least squares errors of tomographic reconstructions of synthetic data with varying LoS with on-axis/off-axis synthetic profiles.

Number of LoSs	Second derivative on-/off-axis	Minimum Fisher on-/off-axis
28	0.026/0.030	0.018/0.028
56	0.003/0.011	0.003/0.011
84	0.001/0.007	0.001/0.007

cameras. These cameras can be housed in the upper and lower diagnostic ports in a manner similar to the current cameras, which are housed in the central port. Tomographic reconstruction is performed on both on-axis and off-axis NBI cases with the additional LoS and with each of the methods previously described. The normalized least squares error of each method is reported in Table I. As expected, there is a significant decrease in the least squares error when additional lines of sight are employed in the reconstruction. The minimum Fisher method reduces the error by a factor of greater than 10 times for the case of 84 LoSs (the current MAST-U SXR LoS combined with the additional 54) for the on-axis NBI case and by a factor of four in the case of off-axis NBI heating.

The reconstructed SXR emissivity with 14 additional upper and lower LoSs is shown in Fig. 7 [panel (a) for the on-axis NBI case and panel (b) for the off-axis case]. Increasing the LoS by 28, going from Figs. 7 and 8, results in an improved reconstruction of both the on-axis NBI case and the off-axis NBI case. The reconstructed emissivity with 84 LoSs is shown in Fig. 8 [panel (a) for the on-axis NBI case and panel (b) for the off-axis case]. The reconstructions with additional LoSs improve upon the reconstructions that employ fewer LoSs. The structure in Figs. 7(b) and 8 can be seen qualitatively with the addition of extra LoSs.

As an additional check on the validity of the reconstruction, the integrated emission of the synthetic emissivity [which was used as f in Eq. (2)] is compared to the integrated emission of the reconstructed image. Figure 9(a) shows the integrated emission from the on-axis case, and Fig. 9(b) shows the integrated emission from the

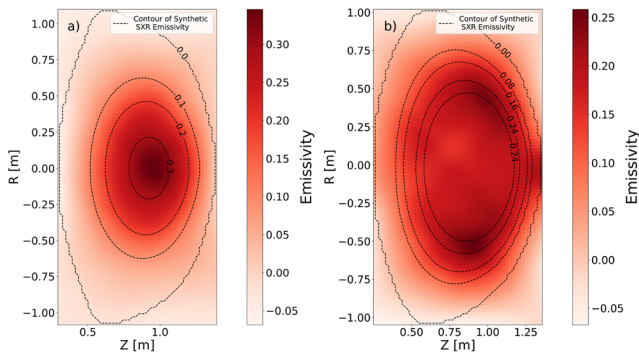


FIG. 7. Two reconstructed SXR emissivity profiles using minimum Fisher smoothing and an additional 14 upper and 14 lower LoSs. Panel (a) features on-axis heating, and panel (b) features off-axis heating. The contours indicate the synthetic emissivity that panels (a) and (b) reconstruct.

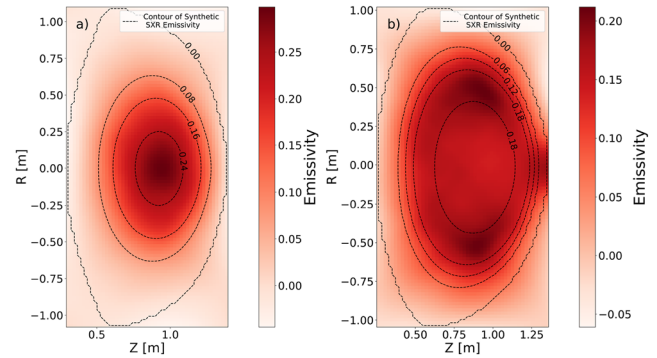


FIG. 8. Two reconstructed SXR emissivity profiles using minimum Fisher smoothing and an additional 28 upper and 28 lower LoSs. Panel (a) features on-axis heating, and panel (b) features off-axis heating. The contours indicate the synthetic emissivity that panels (a) and (b) reconstruct.

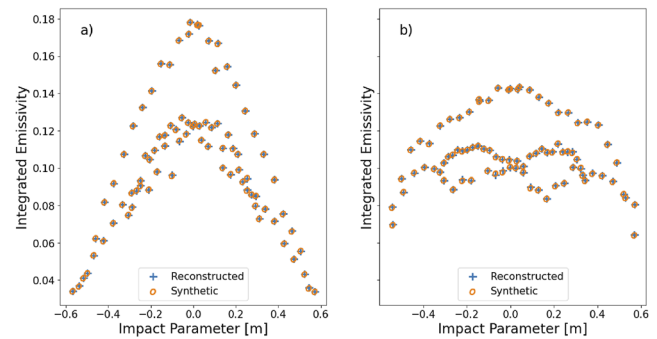


FIG. 9. Emissivity of the synthetic and reconstructed profiles, integrated over the LoS paths in each case. The reconstruction is done with 28 extra lines of sight above and below using the minimum Fisher method. Panel (a) features on-axis heating, and panel (b) features off-axis heating. Here, the impact parameter measures the shortest distance from the geometric axis to a LoS.

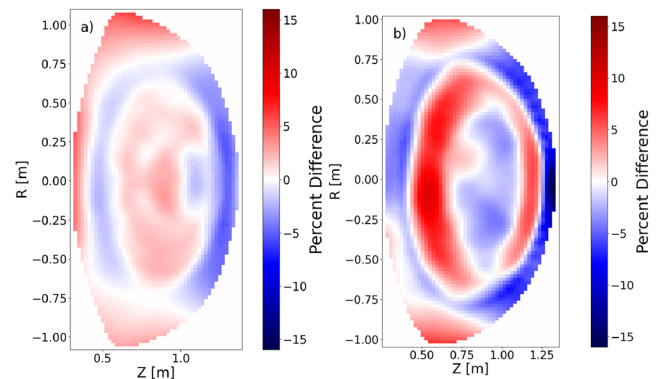


FIG. 10. Percent difference between the synthetic profiles in Fig. 2 and the reconstructions of Fig. 8. Panel (a) features on-axis heating, and panel (b) features off-axis heating.

off-axis case. In both cases, the coefficient of determination between the two integrated emissions is greater than 0.99. This check will become more necessary in future work when the system is used on experimental data, and there will be no emissivity field to check against.

Figure 10(a) shows the percent difference in the synthetic reconstruction in the 84 LoS minimum Fisher reconstruction case when on-axis NBI heating is used. In this case, the percent error peaks at about seven percent. Figure 10(b) shows the same reconstruction method but with the off-axis NBI heating profile. In this case, the maximum error is ~15%. In both figures, there is a central area in which the error is low, followed by a ring structure surrounding the central area in which the error is higher. This is much more pronounced in the off-axis case, due to the error in reconstructing the ring shaped SXR profile.

V. CONCLUSIONS AND FUTURE WORK

The results shown in this work suggest that the addition of intersecting lines of sight to the current SXR diagnostic on MAST-U would lead to vastly improved tomographic reconstructions of SXR emissivity, which can potentially lead to the detection of MHD features and instabilities in the plasmas. The spatial extent of features that can be reconstructed with these techniques will be tested in future work, with an aim to resolve features that are approximately the size of MHD instabilities. Currently, this work shows the potential to discern MHD instabilities with a low poloidal mode number. The limitation on the mode number that can be discerned by this system will be examined.

With these tomographic methods, a synthetic perturbed emissivity will be reconstructed. The amplitudes of these features are particularly important as they will help constrain numerical models of the interaction between fast ions and these MHD perturbations. The significant improvement in SXR emissivity reconstruction that is seen with the additional lines of sight warrants the consideration of a system improvement to add such cameras. Future work in this area will be focused on improving and implementing new tomography techniques, including maximum entropy and machine learning methods. Maximum entropy methods use a minimum of additional information to the system and treat the reconstruction probabilistically using the assertion of an entropic background.¹¹ This method does not correlate adjacent pixels with each other and will therefore not smooth the SXR emissivity in the same way as the second derivative and minimum Fisher information methods presented. This may possibly lead to improved feature detection in the tomographic reconstructions of the emissivity. Machine learning applications will be used to perform a reconstruction of the emissivity from line integrated emissivity profiles. An advantage of using reinforcement learning methods is that it allows non-linearity to be added to the inversion,¹⁴ as opposed to the methods discussed here, which rely on using systems of linear equations to reconstruct the image. The training data for a machine learning model can be supplied by using a large number of calculations modeled on MAST-U runs from the transport code TRANSP. Noise will be added to the synthetic data to more closely simulate real measurements made on potentially noisy detectors. New synthetic lines of sight will also be added above and below to see their effect on the plasma. This has not been implemented in the current work due to the divertor that

is currently blocking those LoSs. Future work will focus on investigating the impact of a small hole in the divertor to let a number of LoSs through. The specific size of hole and heat load impact will be evaluated. Work will be done to create checks on the confidence of the reconstruction, in addition to comparing integrated emissivity, which can be used when there is no synthetic emissivity field to work with. Work may also be done to integrate other diagnostics into the reconstruction of the emissivity.

ACKNOWLEDGMENTS

This work was supported by EPSRC (Grant No. EP/W006839/1).

AUTHOR DECLARATIONS

Conflict of Interest

The authors have no conflicts to disclose.

Author Contributions

B. A. Steward: Conceptualization (equal); Data curation (equal); Formal analysis (lead); Writing – original draft (lead); Writing – review & editing (equal). **M. Cecconello:** Conceptualization (equal); Supervision (lead); Writing – review & editing (equal). **C. Bowman:** Data curation (supporting); Resources (supporting).

DATA AVAILABILITY

The data that support the findings of this study are available from the corresponding author upon reasonable request.

REFERENCES

- W. W. Heidbrink *et al.*, “The effect of the fast-ion profile on Alfvén eigenmode stability,” *Nucl. Fusion* **53**, 093006 (2013).
- W. W. Heidbrink and G. J. Sadler, “The behaviour of fast ions in tokamak experiments,” *Nucl. Fusion* **34**, 535 (1994).
- A. Kirk *et al.*, “Overview of recent physics results from mast,” *Nucl. Fusion* **57**, 102007 (2017).
- M. Cecconello, I. J. Dolby, A. Sperduti, J. Rivero-Rodriguez, G. Ericsson, I. Fitzgerald, S. Y. Allan, J. Voller, B. Honey, B. A. Nizar, S. D. Elmore, and MAST-U team, “First observations of confined fast ions in mast upgrade with an upgraded neutron camera,” *Plasma Phys. Controlled Fusion* **65**, 035013 (2023).
- A. B. Mikhailovskii, “Generalized MHD for numerical stability analysis of high-performance plasmas in tokamaks,” *Plasma Phys. Controlled Fusion* **40**, 1907 (1998).
- C. Cheng and M. Chance, “Nova: A nonvariational code for solving the MHD stability of axisymmetric toroidal plasmas,” *J. Comput. Phys.* **71**, 124–146 (1987).
- I. H. Hutchinson, *Principles of Plasma Diagnostics*, 2nd ed. (Cambridge University Press, 2002).
- L. Garzotti, *Mast Soft X-Ray Cameras* (Private communication, 2011).
- K. G. McClements, J. Young, L. Garzotti, O. Jones, and C. A. Michael, “Abel inversion of soft x-ray fluctuations associated with fast particle-driven fishbone instabilities in mast plasmas,” *Plasma Res. Express* **3**, 034001 (2021).
- M. Anton, H. Weisen, M. J. Dutch, W. v. d. Linden, F. Buhlmann, R. Chavan, B. Marletaz, P. Marmillod, and P. Paris, “X-ray tomography on the TCv tokamak,” *Plasma Phys. Controlled Fusion* **38**, 1849 (1996).

¹¹K. Ertl, W. v. d. Linden, V. Dose, and A. Weller, "Maximum entropy based reconstruction of soft x-ray emissivity profiles in W7-AS," *Nucl. Fusion* **36**, 1477 (1996).

¹²L. C. Ingesson, B. Alper, B. J. Peterson, and J. C. Vallet, "Chapter 7: Tomography diagnostics: Bolometry and soft-x-ray detection," *Fusion Sci. Technol.* **53**, 528–576 (2008).

¹³J. Mlynar, M. Imrisek, V. Weinzettl, M. Odstrcil, J. Havlicek, F. Janky, B. Alper, A. Murari, and J.-E. Contributors, "Introducing minimum Fisher regularisation tomography to AXUV and soft x-ray diagnostic systems of the COMPASS tokamak," *Rev. Sci. Instrum.* **83**, 10E531 (2012).

¹⁴G. Wang, J. C. Ye, and B. De Man, "Deep learning for tomographic image reconstruction," *Nat. Mach. Intell.* **2**, 737–748 (2020).